GEOPHYSICS, VOL. 71, NO. 3 (MAY-JUNE 2006); P. E25–E33, 14 FIGS., 2 TABLES.
10.1190/1.2194515

3D surface-related multiple elimination: Data reconstruction and application to field data

Anatoly Baumstein[1] and Mohamed T. Hadidi[1]

ABSTRACT

The wide success of 2D surface-related multiple elimination (SRME) in attenuating complex multiples in many cases has spurred efforts to apply the method in three dimensions. However, application of 3D SRME to conventional marine data is often impeded by severe crossline aliasing characteristic of marine acquisition geometries. We propose to overcome this limitation using a dip-moveout (DMO)-based procedure consisting of the following steps: resorting the data into common offsets to improve crossline sampling, performing DMO to eliminate azimuth variations in the common-offset domain, and efficiently implementing inverse shot-record DMO to reconstruct densely sampled shot records required for 3D SRME to predict multiples correctly. We use a field data example to demonstrate that the proposed shot reconstruction procedure leads to kinematically accurate reconstruction of primaries but may not be able to simultaneously position multiples correctly. The mispositioning of multiples becomes a problem when second- and higher-order multiples must be predicted. We propose to resolve this difficulty by using a layer-stripping approach to multiple prediction. Alternatively, an approximate algorithm that relies on adaptive subtraction to compensate for inaccurate positioning of predicted multiples can be used. Application of the latter approach is illustrated with a field data example, and its performance is evaluated quantitatively through a measurement of S/N ratio improvement. We demonstrate that a DMO-based implementation of 3D SRME outperforms conventional 2D SRME and can accurately predict and attenuate complex 3D multiples.

INTRODUCTION

Attenuation of surface-related multiples is an important problem that has been studied by many authors (Riley and Claerbout, 1976; Carvalho et al., 1991; Berkhout and Verschuur, 1995; Dragoset and Jeričević, 1998). In particular, surface-related multiple elimination (SRME), as described in Berkhout and Verschuur (1995) and Dragoset and Jeričević (1998), is an effective algorithm that has been applied successfully to a large number of field data sets. A widely used approach for suppressing surface-related multiples in 3D data sets is to perform 2.5D SRME (Matson and Corrigan, 2000; Hadidi et al., 2002). In this technique, an approximate method (such as differential NMO) regularizes and transforms data into a form suitable for application of 2D SRME, based on the assumption that the subsurface does not vary in the crossline direction.

SRME does not assume that the subsurface is laterally invariant in the crossline direction, but its 3D implementation requires additional information to predict multiples — namely, a shot and a receiver at every surface location. Typical marine acquisition geometries deliver much sparser surface coverage than 3D SRME requires, and various approaches to overcoming this problem have been proposed. Levin (2000) use an approximate NMO-based method to perform zero-offset 3D SRME; van Dedem and Verschuur (2002) use sparse inversion to predict 3D multiples; van Borselen et al. (2005) rely on a combination of processing and acquisition solutions; and Kleemeyer et al. (2003), Lin et al. (2004), Matson et al. (2004), and Moore and Dragoset (2004) use a variety of approaches to make application of 3D SRME feasible.

We propose using a dip-moveout (DMO) based reconstruction technique to create the input necessary for 3D SRME. DMO maps all data to zero offset followed by inverse DMO, which reconstructs densely sampled prestack data on a regular grid. We review this method and discuss a robust way to apply it to field data.

Once the necessary data have been reconstructed, 3D SRME can be applied. We highlight several issues associated with using reconstructed data for multiple prediction and present an example of applying our methodology to attenuate complex 3D multiples in

Manuscript received by the Editor November 10, 2004; revised manuscript received September 2, 2005; published online May 24, 2006.
[1]ExxonMobil Upstream Research Company, P.O. Box 2189, Houston, Texas 77252-2189. E-mail: anatoly.i.baumstein@exxonmobil.com; m.t.hadidi@exxonmobil.com.

field data. We compare the results of applying conventional 2.5D SRME and the proposed 3D SRME methodology and derive quantitative measures of S/N improvement in each case.

DATA RECONSTRUCTION

In our approach, data regularization and missing-shot reconstruction form the key first step in preparing data for 3D SRME. A number of interpolation techniques [see Abma and Kabir (2003) for an overview] attempt to interpolate missing data and place irregularly sampled data on a fixed grid. Spatial aliasing is a universal difficulty affecting all existing methods. Although these methods can interpolate data beyond aliasing under certain assumptions, their performance degrades as shot and receiver sampling become coarser and aliasing becomes more severe. Given that typical shot intervals in marine acquisition are hundreds of meters in the crossline direction, the problem of interpolating data to make it suitable for 3D SRME, which requires a data spacing of roughly 10–20 m to avoid aliasing during multiple prediction, still presents a considerable challenge.

Conceptually, if the subsurface properties are known, one should be able to reconstruct seismic data at arbitrary locations through modeling. However, this is not easy to achieve in practice since subsurface velocities and densities are typically not known with sufficient accuracy. A more practical approach to overcoming aliasing is to sort data into common offsets, where both inline and crossline sampling are typically much finer, map data to zero offset with the help of DMO, and reconstruct the desired shot-receiver geometry by performing inverse mapping to finite offset with the help of inverse common-offset DMO. Although this approach makes certain simplifying assumptions about wavefield propagation, it has been used successfully to regularize marine data and serves as the basis of azimuth moveout (AMO) (Biondi et al., 1998) The key issue in the case of the shot-record interpolation problem is that the output shot records comprise a wide range of azimuths and offsets. While AMO is an efficient way of rotating irregular prestack data to a single common azimuth and offset, one would have to perform a large number of AMO runs to reconstruct all possible azimuths and offsets that might be present in a shot record, leading to an expensive approach. An alternative is a general data reconstruction method (Stolt, 2002), which can map arbitrary input shot geometry into regular output shot geometry.

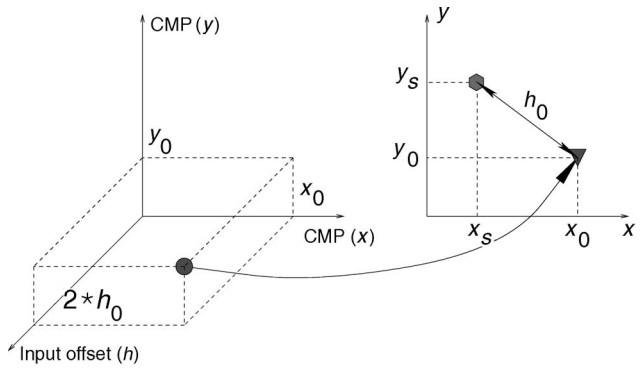

Figure 1. Procedure for forming input to ISR DMO. The left side shows zero-offset data after common-offset DMO. The right side shows a zero-offset shot record that serves as input to ISR DMO. Given a shot (hexagon) location (x_s, y_s), the trace (triangle) at location (x_0, y_0), a distance of h_0 away, is obtained by selecting a trace (circle) with offset $2h_0$ from the common-midpoint (CMP) gather located at (x_0, y_0).

Table 1. Acquisition parameters.

Parameter	Value
Number of streamers	8
Streamer length	5 km
Streamer spacing	100 m
Group spacing	12.5 m
Number of sources	2
Separation between sources	50 m
Shot interval	37.5 m, flip-flop

We prefer a two-step approach comprising forward common-offset DMO followed by inverse shot record (ISR) DMO (Baumstein, 2004; Baumstein et al., 2005). (For completeness, the derivation of ISR DMO is reproduced in Appendix A.) The two-step approach has a number of advantages. First, the forward DMO step can compensate for irregular acquisition geometry (Beasley and Klotz, 1992). Second, once the data have been mapped to zero offset and azimuth variations are no longer present, missing data can be interpolated more easily. Finally, the last step (ISR DMO) has regularized data as its input and can be implemented efficiently in the Fourier domain with the help of a log-stretch transformation (Baumstein, 2004). In addition, the geometry and locations of the reconstructed shots can be chosen dynamically to satisfy the requirements of 3D SRME.

In principle, for a constant-velocity medium, a single well-sampled common-offset section produced by forward common-offset DMO is all that ISR DMO would need to reconstruct shot records at arbitrary locations. However, for field data, it is very important to take advantage of data redundancy to reduce the method's sensitivity to errors in NMO velocities and deviations from hyperbolic moveout. We achieve this by using multiple common-offset sections after DMO as input to ISR DMO (Baumstein and Hadidi, 2004). The idea behind our approach is that because the subsurface dips are not known a priori, the input to ISR DMO should be formed by choosing traces that are the most appropriate for a subsurface consisting of flat layers. This means that when forming a zero-offset shot-record cube (to serve as input to ISR DMO) from zero-offset panels after forward DMO, we select traces with matching midpoint locations that came from the most appropriate input offset, as explained in Figure 1. The resulting reconstruction procedure is kinematically accurate for all dips and is robust with respect to NMO velocity errors. Of course, performing forward DMO in common offsets is a matter of convenience and not a requirement. Our method would work equally well if forward DMO were performed in shot records. In this case, several nearby post-DMO shot records would contribute to each ISR DMO input cube.

We tested the accuracy of our method using a field data set, which was acquired using a racetrack acquisition pattern with a dual-source, eight-streamer configuration. Acquisition geometry details are summarized in Table 1. We first performed reconstruction at a location where a shot had been acquired in the field. While it may seem that reconstructing data at a location where actual field

data were acquired is an easy task, it turns out that our reconstruction technique, which involves common-offset processing, generally treats all surface locations equally, regardless of whether a shot was actually acquired at a particular location. Moreover, it is almost immaterial whether a particular shot was used during the reconstruction process because it constitutes a tiny fraction of the data contributing to a particular common-offset cube. Therefore, we expect the quality of reconstruction to be similar at all surface locations and can verify the accuracy of our method by comparing reconstructed data with the colocated field data. The reconstructed shot has regular dense receiver coverage, while the corresponding field shot record has receivers distributed along eight streamers affected by feathering.

Figures 2 and 3 compare traces along two streamers from a field shot and the corresponding traces interpolated from the reconstructed shots. NMO has been applied to both shot records to emphasize the complexity of the area. Indeed, the water bottom and subsequent horizons have substantial moveout and curvature even after applying NMO on account of significant dips in both inline and crossline directions. Despite the complexity, key primary events have been reconstructed accurately. Multiples, on the other hand, have been mispositioned because their NMO velocities differ from those of the primaries, so DMO is unable to position both of them correctly at the same time. (In the next section we discuss the implications of this fact for multiple prediction.) Note that the reconstructed shot records appear to be less noisy than the corresponding field data. This is a result of applying f–x-domain noise attenuation prior to DMO to prevent random noise from turning into coherent DMO smiles, which in turn can have a detrimental effect on the quality of multiple prediction. The amount of random noise suppression must be balanced against the need to preserve weak and steeply dipping events, some of which have not been reconstructed in this case.

We can get a different perspective on the reconstruction quality by comparing time slices from the field and reconstructed data sets. To make the time-slice comparison more informative by including as many events as possible in a single time slice, we did not apply NMO in this case. Figure 4 shows a time slice from the same field shot record. Eight streamers used in acquisition can be identified easily. Figure 5 shows the same time slice from the reconstructed shot record. We can evaluate whether spatially continuous features visible in Figure 5 agree with data recorded in the field by examin-

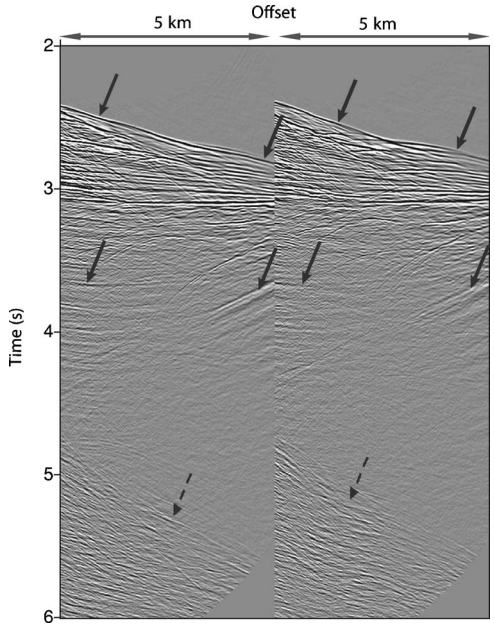

Figure 2. Field data, (left) far and (right) near streamers. Solid arrows point to primaries that have been correctly positioned by the reconstruction procedure. Dashed arrows point to multiples that are mispositioned in the reconstructed data in Figure 3.

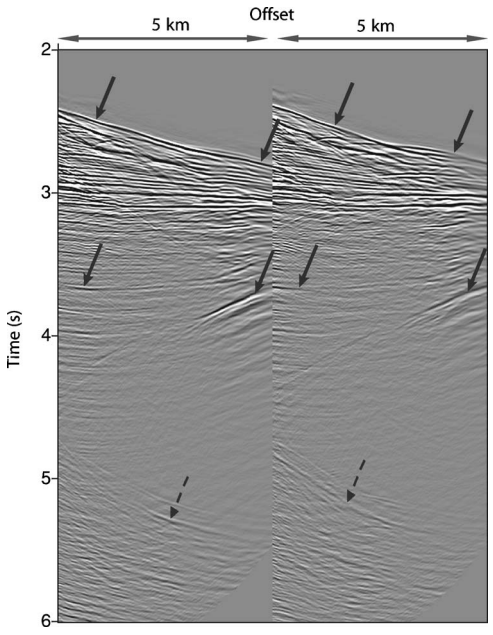

Figure 3. Reconstructed data, (left) far and (right) near streamers. Solid arrows point to primaries that have been correctly positioned by the reconstruction procedure. Dashed arrows point to mispositioned multiples.

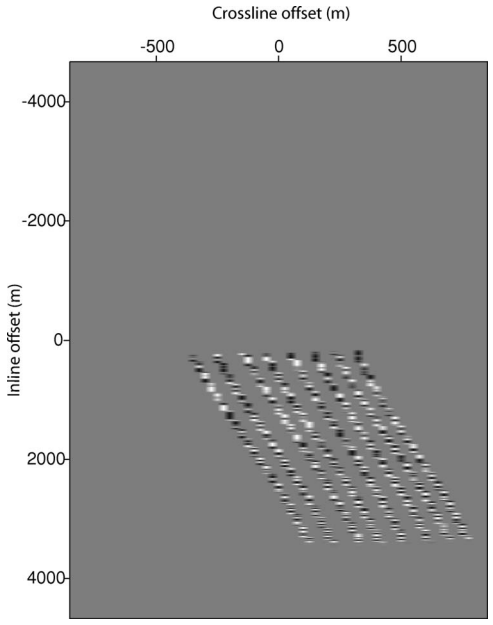

Figure 4. Field data; time slice at $t = 3.5$ s. Note that streamer feathering appears exaggerated as a result of the aspect ratio of the plot.

ing the overlay of field data on the reconstructed data shown in Figure 6. Observe that reconstructed events match field data quite well.

To perform 3D SRME, we need to reconstruct densely sampled shot records at every surface location where a shot or a receiver was present in the field. Because of feathering and other acquisition irregularities, these locations would not adhere to a regular pattern and would cover the surface almost continuously. To avoid reconstructing an immense amount of data, we generated densely sampled shot records on a regular 25 × 25 m grid and then used on-the-fly interpolation to form gathers at the exact source and receiver locations for each trace. The reconstructed shot gathers had inline offsets that ranged from −5 to + 5 km and crossline offsets that ranged from −1 to + 1 km. The crossline offset range was a compromise between our desire to use the widest possible crossline aperture during 3D multiple prediction and the need to minimize the amount of data being reconstructed. Several techniques [e.g., Moore and Dragoset (2004) and Baumstein et al. (2005)] can be used to estimate the required crossline aperture based on some assumption about the nature of the multiples. We use the method described in Baumstein et al. (2005), which makes a prediction based on the kinematics of the first-order, zero-offset water-bottom multiple.

MULTIPLE SUPPRESSION

Once the necessary data have been reconstructed, we can perform 3D SRME. It can be applied to the reconstructed data or to the original field data, with the reconstructed data used to obtain a prediction of multiples at the locations of the original field data traces. We prefer the second approach; if the reconstructed data are used for multiple prediction and then discarded, we can allow ourselves greater flexibility in handling amplitudes and steep dips.

Because our reconstruction method is DMO based, it cannot correctly reconstruct primaries and multiples simultaneously. It is therefore desirable to first identify the multiple-free portion of the data (i.e., the region between the water bottom and the first-order water-bottom multiple) and then carry out the reconstruction process described in the previous section. First-order multiples can be predicted using the reconstructed primaries and attenuated in the original field data. To predict second-order multiples, we would need to convolve primaries with first-order multiples, both of which should be available in the form of regularly spaced and densely sampled shot records. Regularized first-order multiples can be obtained through DMO-based reconstruction of the multiples subtracted in the previous step. Such reconstruction has a good chance of being accurate: Multiples are now separated from primaries, so appropriate NMO velocities can be used. Alternatively, regularized first-order multiples can be obtained through convolution of the reconstructed primaries. The two data sets (primaries and multiples) can be convolved with each other to obtain a prediction of the second-order multiples. The process is then repeated for higher-order multiples as many times as necessary.

This recursive process requires considerable human input to identify the multiple-free portion of the data and significant computer resources to perform repeated data reconstructions and convolutions. Human intervention can be held to a minimum for the case of a relatively flat water bottom, where 3D effects are from either diffracted multiples or mild crossline undulations of the water bottom. The amount of computation to be performed in the second and subsequent iterations can be reduced in two ways. First, we only need to reconstruct those primaries that were previously obscured by multiples and reuse regularized primaries from the multiple-free region of the previous iteration. Second, we can choose whether to compute lower-order regularized multiples (required for predicting higher-order multiples) at the shot or receiver locations. The number of shot locations is typically an order of magnitude smaller than the number of receiver locations; so if the

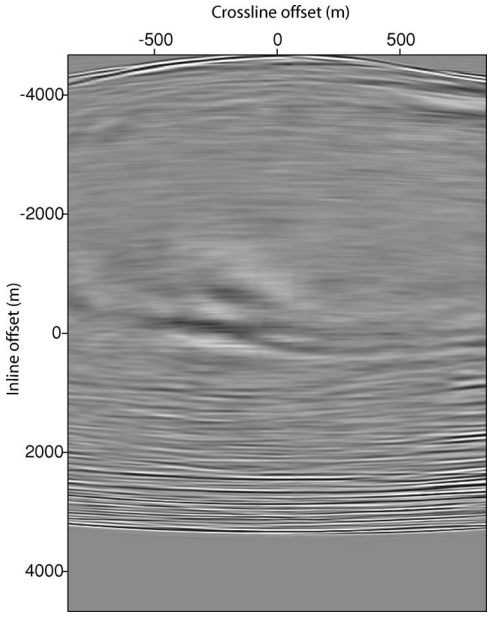

Figure 5. Reconstructed data; time slice at t = 3.5 s.

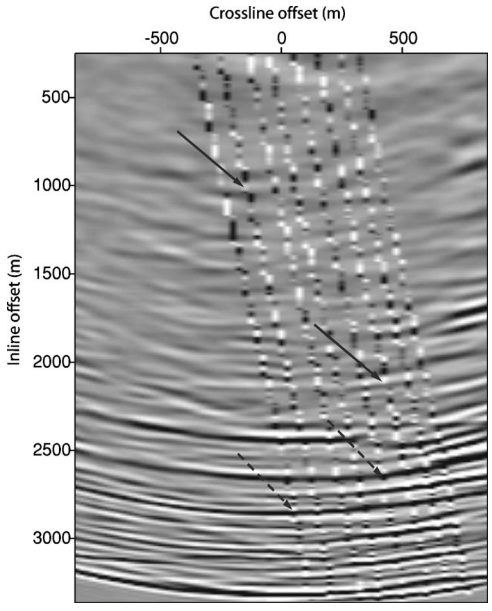

Figure 6. Field data overlaid on reconstructed data. Only a subset of the larger area shown in Figures 4 and 5 is displayed here. Solid arrows point to examples of areas with perfect positioning, while dashed arrows point to events that have been slightly mispositioned. The mispositioning is about one sample (4 ms) if viewed in the vertical time-offset plane.

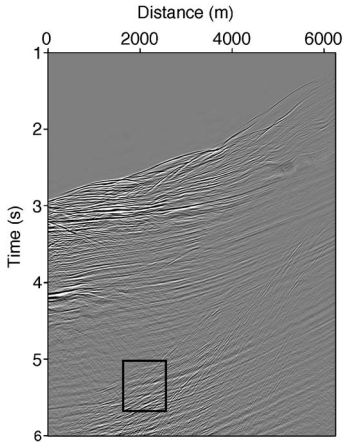

Figure 7. Input stack. The area inside the rectangle was used for quantitative evaluation of the degree of multiple suppression.

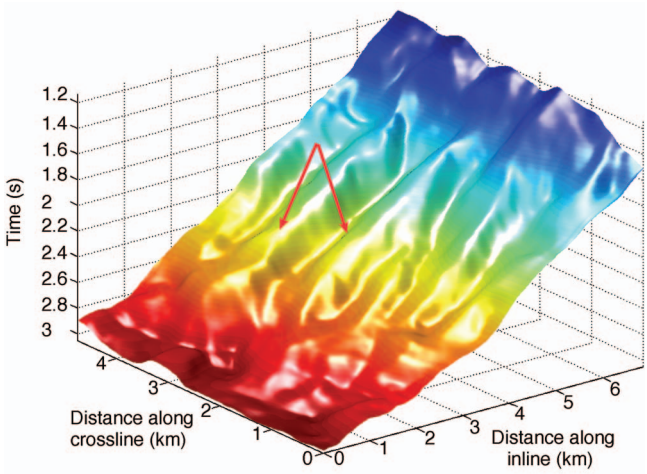

Figure 8. Water-bottom map. The arrows point to crossline undulations of the water bottom, the primary cause of 3D multiples.

implementation of reconstruction is more efficient than that of convolution, we would want to use convolution to compute multiples at the shot locations and perform data reconstruction for the primaries in the expanded multiple-free region at receiver locations.

When the recursive procedure is impractical or if only lower-order multiples need to be suppressed, a simplified method can be used: We reconstruct not only the multiple-free portion of the data but also the part of the data contaminated by multiples. Positioning of reconstructed multiples will not be entirely correct but can be accepted as an approximation. The reconstructed data are used to perform convolutions and predict multiples to all orders simultaneously. This is the approach we use in the examples below.

Figure 7 shows a stacked section from the same field data set used in the data reconstruction section. The multiples are 3D in nature and were caused by crossline undulations of the water bottom (Figure 8). We first applied 2.5D SRME (Figure 9a); it suppressed some of the multiples (Figure 9b), but, as expected, its effectiveness was limited. The reason is that 2.5D SRME relies on differential NMO to regularize data by compensating for offset (but not azimuth) irregularities in shot gathers and then performs 2D multiple prediction on a streamer-by-streamer basis. As a result, it is unable to correctly account for 3D effects because of either subsurface geology or streamer feathering, both of which were present in our data. Next, we applied 3D SRME; it performed considerably better (Figures 9c and 9d). The 3D effects can be ob-

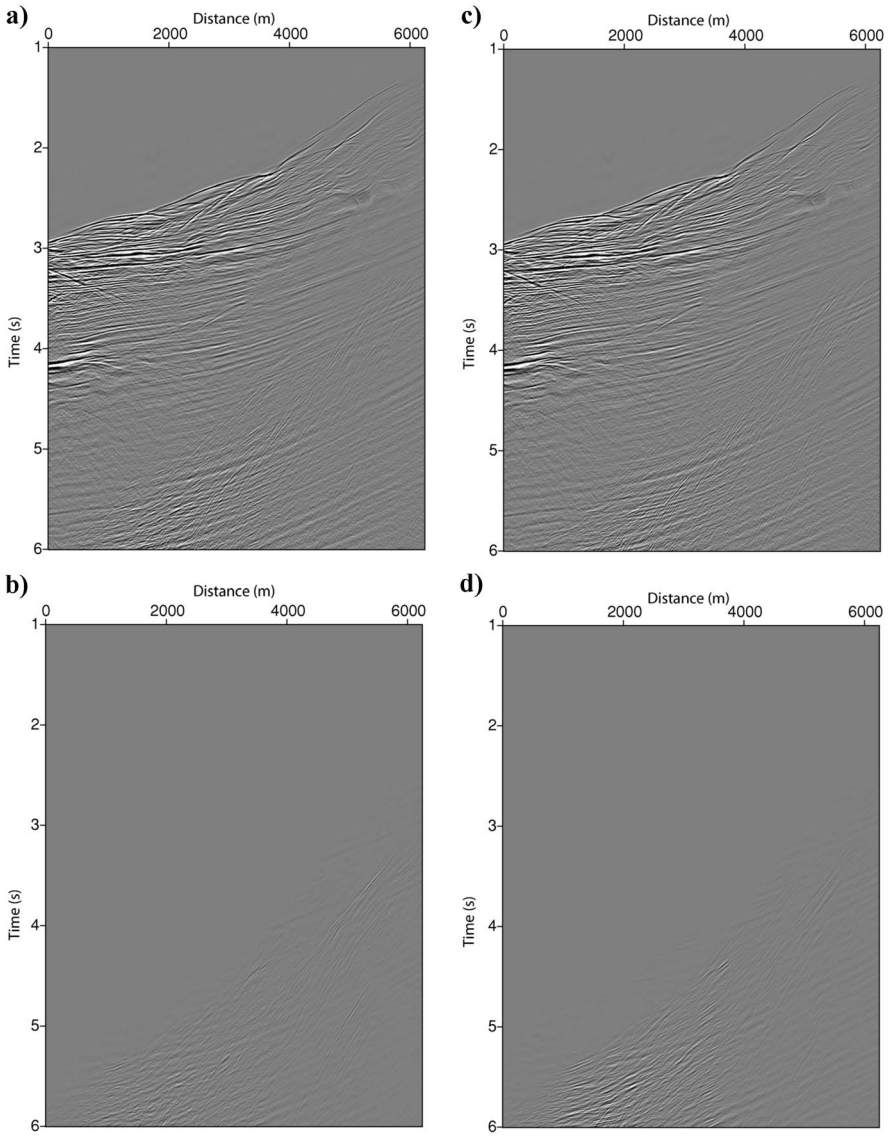

Figure 9. (a) 2.5D SRME stack. (b) Difference between input and 2.5D SRME stacks. (c) 3D SRME stack. (d) Difference between input and 3D SRME stacks.

served in the crossline multiple contribution gathers (MCGs) produced by 3D SRME, as shown in Figure 10. Each one of the four gathers in Figure 10 is the result of trace-by-trace time-domain convolution of two densely sampled gathers (centered at the shot and receiver positions of a given trace), followed by a stack in the inline direction. The apex location in each of the moveout curves corresponds to the crossline position of the downward reflection points on the free surface. The extent to which these locations are displaced from the center of the gather determines the crossline aperture that should be used in 3D SRME to predict and attenuate multiples correctly. We use a crossline half-aperture of approximately 750 m, which is sufficient to attenuate many, but not all, multiples. The size of the crossline aperture is a compromise between the desire to account for all 3D effects and the need to control processing cost (which is proportional to the aperture used).

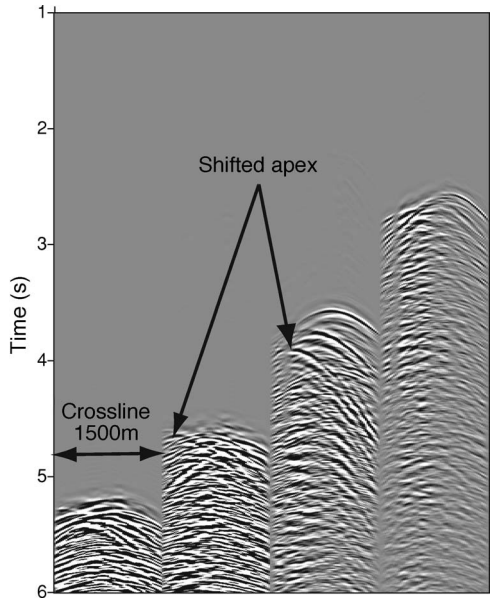

Figure 10. Crossline multiple-contribution gathers at select locations.

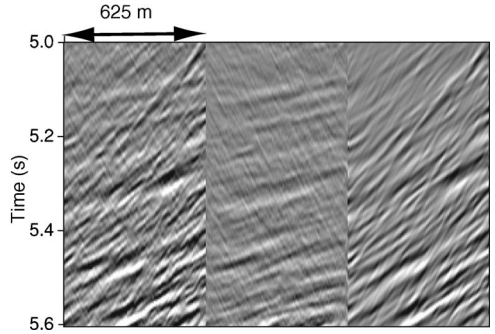

Figure 11. Decomposition of the data into signal and noise components. (left) Data (primaries and multiples). (middle) Primaries, which are subhorizontal. (right) Multiples dipping at a steep angle.

Table 2. Quantitative evaluation of multiple suppression results.

Stack	Signal	Noise	S/N ratio, %	S/N ratio increase, %
Raw	9.07	16.04	56.546	
2.5D SRME	8.05	13.65	58.974	4.29
3D SRME	7.95	10.61	74.929	32.51

To quantify our assessment of the multiple suppression quality, we measured the amount of S/N improvement in a small window depicted in Figure 7. The window was chosen to include both signal (primaries) and noise (multiples) that could be discriminated by their dip. Notice that primaries are mostly flat, while multiples dip at a considerable angle. We used a linear τ-p transform to decompose the data within each window into signal and noise (Figure 11) and computed the amount of energy (rms amplitude) in the window for each component before and after multiple attenuation.

The results are summarized in Table 2. The second column in Table 2 is the signal (primaries) amplitude in the raw stack and after 2.5D and 3D SRME, respectively. The third column is the noise (multiples) amplitude of the same three stacks. The fourth column is the S/N ratio expressed as a percentage. The last column shows the amount of improvement in SNR from multiple suppression. Because of imperfect separation between signal and noise in the τ-p decomposition, there is still some multiple energy left in the signal, which largely accounts for the fact that signal content decreases after multiple suppression (Table 2, column two). By examining the last column, we can see that the application of 2.5D SRME led to a modest increase in SNR of approximately 4%, while 3D SRME improved SNR by 32%. Although the exact level of SNR increase varies spatially and depends on the choice of analysis window, the application of 3D SRME improved overall interpretability.

CONCLUSIONS

We have discussed a sequence of processing steps that enables successful application of 3D SRME to conventional marine data. Our DMO-based data reconstruction approach is a robust way to overcome spatial aliasing and reconstruct the data required for application of 3D SRME, which can be applied to both heritage and newly acquired data. We have demonstrated with a field data example that the accuracy of DMO-based data reconstruction is sufficient to significantly improve attenuation of complex 3D multiples.

Additional topics that need to be explored include determination of optimal sampling to be used in acquisition, data reconstruction, 3D SRME application, simultaneous accurate reconstruction of primaries and multiples, and alternative data reconstruction approaches.

ACKNOWLEDGMENTS

We would like to thank ExxonMobil Upstream Research Company for permission to publish this work. We are grateful to T. A. Dickens, D. L. Hinkley, K. T. Lewallen, E. Neumann, and W. S. Ross for many useful discussions. We appreciate many insightful comments and constructive suggestions by the anonymous reviewers and the associate editor.

APPENDIX A
ISR DMO

This appendix presents a derivation of the inverse shot record (ISR) DMO, a key component of our data reconstruction methodology.

Derivation of Fourier-domain ISR DMO

Since DMO is a line (2D) operator, we carry out the derivation in two dimensions with subsequent generalization to three dimensions. Figure A-1 depicts the geometry necessary to derive the ISR DMO operator. In the figure, S and R are the shot and receiver locations, respectively; S' is the mirror image of the shot with respect to the dipping reflector; OQ is the dipping reflector, with Q being the reflection point; β and α are the dip and reflection angles; Z is the zero-offset reflection location; $d_0 = vt_0/2$ is the distance from Z to the reflection point; d_S is the distance from the source S to the reflector; t_0 is the two-way zero offset traveltime; and t_S and t_R are the one-way traveltimes from the reflection point to the source and receiver, respectively.

Consider $\Delta OS'R$. From the law of cosines

$$\begin{aligned} v^2t^2 &= v^2(t_S + t_R)^2 = |S'R|^2 \\ &= |OS'|^2 + |OR|^2 - 2|OS'||OR|\cos 2\beta \\ &= (|OS'| - |OR|)^2 + 4|OS'||OR|\sin^2\beta \\ &= (|OR| - |OS|)^2 + 4|OS||OR|\sin^2\beta \\ &= h^2 + 4|OS||OR|\sin^2\beta, \end{aligned}$$

where $h = |OR| - |OS|$ is the source-receiver offset. Performing NMO gives

$$\begin{aligned} t_n^2 &= t^2 - \frac{h^2}{v^2} \\ &= \frac{4\sin^2\beta}{v^2}|OS||OR| \\ &= \frac{4\sin^2\beta}{v^2}\left(\frac{d_0}{\sin\beta} - h_0\right)\left(\frac{d_0}{\sin\beta} - h_0 + h\right), \end{aligned} \quad \text{(A-1)}$$

where $h_0 = |SZ|$ is the distance from the shot to the location of the zero-offset arrival from reflection point Q.

Now consider ΔSZQ and ΔRZQ and apply the law of sines:

$$\frac{h_0}{\sin\alpha} = \frac{d_0}{\cos(\beta - \alpha)},$$

$$\frac{h - h_0}{\sin\alpha} = \frac{d_0}{\cos(\beta + \alpha)}.$$

Therefore,

$$h = h_0\frac{d_0 - h_0\sin\beta}{\frac{d_0}{2} - h_0\sin\beta}. \quad \text{(A-2)}$$

Substituting equation A-2 into equation A-1, we get

$$t_n^2 = 4\frac{d_0}{v^2}\frac{(d_0 - h_0\sin\beta)^2}{d_0 - 2h_0\sin\beta} = \frac{4d_s^2}{v^2}\frac{1}{1 - 2\frac{h_0}{d_0}\sin\beta}. \quad \text{(A-3)}$$

Equations A-2 and A-3 allow us to compute h and t_n in terms of h_0, t_0, v, and β. While h_0 and t_0 are known properties of the input zero-offset dataset, β is the subsurface reflector dip and is not known in advance. Similarly to the approach taken in the derivation of any DMO operator, we eliminate dependence on the unknown geologic dip β (and, as it turns out, medium velocity v) by going to the Fourier domain. Differentiating equation A-1 with respect to h and using $\partial t_n/\partial h = k_h/\omega_n$, we obtain

$$t_n = \frac{2d_s}{v}\frac{\omega_n}{k_h}\frac{\sin\beta}{v}, \quad \text{(A-4)}$$

where ω_n and k_h are the Fourier-domain variables corresponding to t_n and h. Introducing

$$\rho = \frac{h_0\sin\beta}{vt_0}, \quad \text{(A-5)}$$

$$\gamma = \frac{k_h h_0}{\omega_n t_0}, \quad \text{(A-6)}$$

and combining equations A-3 and A-4, we obtain the following equation for ρ as a function of γ:

$$\rho\sqrt{1 - 4\rho} = \gamma. \quad \text{(A-7)}$$

Rewriting equations A-2 and A-3 in terms of ρ and γ, we get

$$h(t_0, h_0) = h_0\frac{4\rho - 2}{4\rho - 1}, \quad \text{(A-8)}$$

$$t_n(t_0, h_0) = t_0\frac{\rho}{\gamma}(1 - 2\rho). \quad \text{(A-9)}$$

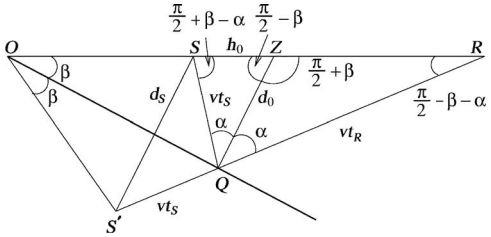

Figure A-1. Dipping reflector in a constant-velocity medium.

Equations A-6 through A-9 allow us to compute t_n and h given t_0, h_0, ω_n, and k_h.

We are now ready to formulate Fourier-domain ISR DMO. Let $P_n(t_n,h)$ denote a shot record after NMO, $\hat{P}_n(\omega_n,k_h)$ denote its Fourier transform, and $P_0(t_0,h_0)$ denote a zero offset section. Then

$$\begin{aligned}\hat{P}_n(\omega_n,k_h) &= \int\int e^{i(\omega_n t_n - k_h h)} P_n(t_n,h)\mathrm{d}t_n\mathrm{d}h \\ &= \int\int e^{i(\omega_n t_n(t_0,h_0) - k_h h(t_0,h_0))} P_0(t_0,h_0) \\ &\quad \times J(t_n,h;t_0,h_0)\mathrm{d}t_0\mathrm{d}h_0. \end{aligned} \tag{A-10}$$

To evaluate the Jacobian J, we first need to compute several auxiliary expressions. From equation A-6 we get

$$\frac{\partial\gamma}{\partial t_0} = -\frac{\gamma}{t_0}, \tag{A-11}$$

$$\frac{\partial\gamma}{\partial h_0} = \frac{\gamma}{h_0}. \tag{A-12}$$

Using these expressions in combination with equation A-7, we also get

$$\frac{\partial\rho}{\partial t_0} = \frac{\gamma}{\rho(1-6\rho)}\frac{\partial\gamma}{\partial t_0} = -\frac{\rho(1-4\rho)}{t_0(1-6\rho)}, \tag{A-13}$$

$$\frac{\partial\rho}{\partial h_0} = \frac{\gamma}{\rho(1-6\rho)}\frac{\partial\gamma}{\partial h_0} = \frac{\rho(1-4\rho)}{h_0(1-6\rho)}. \tag{A-14}$$

The four entries of the Jacobian matrix can be now computed using equations A-8 through A-14

$$\frac{\partial t_n}{\partial t_0} = \frac{\rho - 8\rho^2 + 8\rho^3}{\gamma(1-6\rho)},$$

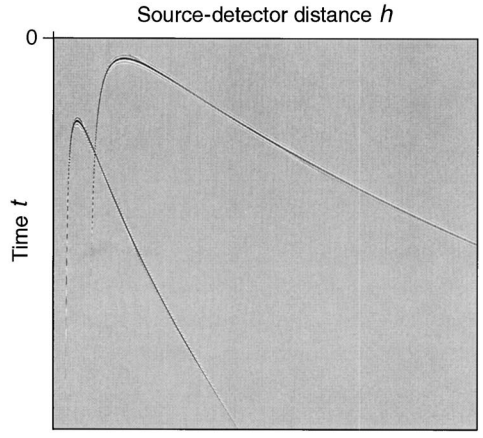

Figure A-2. Impulse responses (computed using equation A-10) for two different impulse locations. Note change of operator shape with location.

$$\frac{\partial t_n}{\partial h_0} = \frac{t_0}{h_0}\frac{4\rho^3}{\gamma(1-6\rho)},$$

$$\frac{\partial h}{\partial t_0} = -\frac{h_0}{t_0}\frac{4\rho}{(1-4\rho)(1-6\rho)},$$

$$\frac{\partial h}{\partial h_0} = 2\frac{1-6\rho+12\rho^2}{(1-4\rho)(1-6\rho)}.$$

Finally, we obtain

$$J(t_n,h;t_0,h_0) = \frac{\partial(t_n,h)}{\partial(t_0,h_0)} = \frac{2\rho(1-2\rho)^2}{\gamma(1-6\rho)}.$$

An important question that remains to be answered (and is outside the scope of this paper) is whether this expression for the Jacobian leads to a true-amplitude formulation.

An aperture limitation can be derived from equation A-5:

$$|\rho| = \left|\frac{h_0 \sin\beta}{v t_0}\right| \le \left|\frac{h_{0\,\max}\sin\beta_{\max}}{v_{\min} t_{0\,\min}}\right|,$$

where $\beta_{\max}$, $h_{0\,\max}$, $v_{\min}$, and $t_{0\,\min}$ are the maximum and minimum values of the respective parameters in a given data set.

Combining equations A-7, A-8, and A-9, we get the following equation describing the kinematics of ISR DMO:

$$\left(\frac{2h_0}{h} - 1\right)^2 + \left(\frac{t_0}{t_n}\right)^2 = 1. \tag{A-15}$$

Note that the shape of the operator changes depending on the location of the impulse (see Figure A-2). Therefore, a straightforward implementation of ISR DMO requires repeated computation of the operator and is inefficient.

ISR DMO in the log-stretch domain

Similarly to the conventional shot-record DMO (Biondi and Ronen, 1987; Zhou et al., 1995; Masjukov, 2003) ISR DMO can be implemented as a convolutional operator after a log-stretch transformation:

$$t_n = t_1 \exp\frac{\tau_n}{t_1}, \quad t_0 = t_1 \exp\frac{\tau_0}{t_1},$$

$$h = h_1 \exp\frac{\eta}{h_1}, \quad h_0 = h_1 \exp\frac{\eta_0}{h_1},$$

where t_1 and h_1 serve as the origin of the log-stretch transformations and are usually set equal to the minimum time and offset of interest. Equation A-15 becomes

$$\left(2\exp\frac{\eta_0-\eta}{h_1} - 1\right)^2 + \exp\frac{2(\tau_0-\tau_n)}{t_1} = 1. \tag{A-16}$$

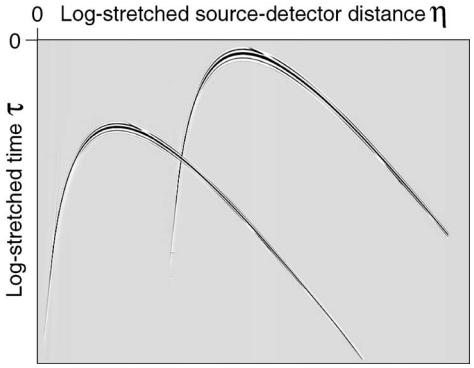

Figure A-3. Impulse responses for two different impulse locations in the log-stretch domain. Operator shape does not vary with location.

We can see from equation A-16 that in the log-stretch domain the ISR DMO operator becomes spatially invariant, as shown in Figure A-3. Therefore, ISR DMO can be implemented as a convolutional operator in offset and time, which in turn allows for a fast implementation in the Fourier domain.

Generalization to three dimensions

To generalize our expressions to three dimensions, we use the fact that DMO is a 2D operator that should lie in the vertical plane passing through the source, midpoint, and receiver locations. Therefore,

$$\frac{h_x}{h_{0x}} = \frac{h_y}{h_{0y}} = \frac{|\vec{h}|}{|\vec{h}_0|}. \tag{A-17}$$

In the log-stretch domain this translates into

$$\eta_y - \eta_{0y} = \frac{h_{1y}}{h_{1x}}(\eta_x - \eta_{0x}). \tag{A-18}$$

We reinterpret equation A-16 as an equation for η_x and η_{0x}. In the log-stretch domain the ISR DMO azimuth is fixed, thus enabling us to reconstruct all azimuths in a shot record at once and to implement 3D ISR DMO as a convolution.

A practical procedure for computing a Fourier-domain ISR DMO operator is as follows:

1) Select a location for the impulse. A good choice is to set $(t_0,h_0) = (t_1,h_1)$ so that $\eta_0 = \tau_0 = 0$.
2) Compute the 2D impulse response $P_{2D}(t_n,h;t_0,h_0)$ according to equation A-10.
3) Perform numeric log-stretching to obtain $P^{\log}_{2D}(\tau_n,\eta)$.
4) Rotate the 2D impulse response $P^{\log}_{2D}(\tau_n,\eta)$ to its correct position in three dimensions according to equation A-18:

$$P^{\log}_{3D}(\tau_n,\eta_x,k_{\eta_y}) = \exp\left(-ik_{\eta_y}\frac{h_{0y}}{h_{0x}}\eta_x\right)P^{\log}_{2D}(\tau_n,\eta_x).$$

5) Fourier-transform $P^{\log}_{3D}(\tau_n,\eta_x,k_{\eta_y})$ in τ_n,η_x to obtain an ISR DMO operator $P^{\log}_{3D}(\omega_n,k_{\eta_x},k_{\eta_y})$.

Note that the ISR DMO operator is invariant with respect to the sign of offset and is applied separately in each quadrant: $(h_x > 0, h_y > 0)$, … ,$(h_x < 0, h_y < 0)$.

REFERENCES

Abma, R., and N. Kabir, 2003, Comparisons of interpolation methods in the presence of aliased events: 73rd Annual International Meeting, SEG, Expanded Abstracts, 1909–1912.

Baumstein, A., 2004, 3D inverse shot record DMO: A tool for shot-domain data regularization: 74th Annual International Meeting, SEG, Expanded Abstracts, 2001–2004.

Baumstein, A., and M. T. Hadidi, 2004, 3D SRME: Data reconstruction and application to field data: 74th Annual International Meeting, SEG, Expanded Abstracts, 1253–1256.

Baumstein, A., M. T. Hadidi, D. L. Hinkley, and W. S. Ross, 2005, A practical procedure for application of 3D SRME to conventional marine data: The Leading Edge, **24**, 254–258.

Beasley, C. J., and R. Koltz, 1992, Equalization of DMO for irregular spatial sampling: 54th Annual Meeting, EAGE, Extended Abstracts, 232–233.

Berkhout, A. J., and E. J. Verschuur, 1995, Estimation of multiple scattering by iterative inversion, part 1: Theoretical considerations: 65th Annual International Meeting, SEG, Expanded Abstracts, 715–718.

Biondi, B., and J. Ronen, 1987, Dip moveout in shot profiles: Geophysics, **52**, 1473–1482.

Biondi, B., S. Fomel, and N. Chemingui, 1998, Azimuth moveout for 3-D prestack imaging: Geophysics, **63**, 574–588.

Carvalho, P. M., A. B. Weglein, and R. H. Stolt, 1991, Examples of a nonlinear inversion method based on the T matrix of scattering theory: Application to multiple suppression: 61st Annual International Meeting, SEG, Expanded Abstracts, 1319–1322.

Dragoset, W. H., and Ž. Jeričević, 1998, Some remarks on surface multiple attenuation: Geophysics, **63**, 772–789.

Hadidi, M. T., A. I. Baumstein, and Y. C. Kim, 2002, Surface-related multiple elimination on wide-tow marine data: The Leading Edge, **21**, 787–790.

Kleemeyer, G., S. E. Pettersson, R. Eppenga, C. J. Haneveld, J. Biersteker, and R. D. Ouden, 2003, It's MAGIC: Industry first 3D surface multiple elimination and pre-stack depth migration on Ormen Lange: 65th Annual International Meeting, EAGE, Extended Abstracts.

Levin, S. A., 2002, Prestack poststack 3D multiple prediction: 72nd Annual International Meeting, SEG, Expanded Abstracts, 2110–2113.

Lin, D., J. Young, Y. Huang, and M. Hartmann, 2004, 3D SRME application in the Gulf of Mexico: 74th Annual International Meeting, SEG, Expanded Abstracts, 1257–1260.

Masjukov, A. V., 2003, 3D F-K and finite-difference dip moveout in cross-spreads: Geophysical Prospecting, **51**, 333–345.

Matson, K., and D. Corrigan, 2000, A 2.5D method for attenuating free-surface multiples based on inverse scattering series: Offshore Technology Conference, http:\\www.otcnet.org.

Matson, K. H., S. Michell, R. Abma, E. Shoshitaishvili, M. C. Williams, I. Ahmed, J. D. Oldroyd, and R. R. Fisher, 2004, Advanced subsalt imaging and 3D surface multiple attenuation in Atlantis: A case study: 74th Annual International Meeting, SEG, Expanded Abstracts, 1269–1272.

Moore, I., and W. H. Dragoset, 2004, Practical, 3D surface-related multiple prediction (SMP): 74th Annual International Meeting, SEG, Expanded Abstracts, 1249–1252.

Riley, D. C., and J. F. Claerbout, 1976, 2-D multiple reflections: Geophysics, **41**, 592–620.

Stolt, R. H., 2002, Seismic data mapping and reconstruction: Geophysics, **67**, 890–908.

van Borselen, R. G., M. A. Schonewille, and R. F. Hegge, 2005, 3D surface-related multiple elimination: Acquisition and processing solutions: The Leading Edge, **24**, 260–268.

van Dedem, E. J., and D. J. Verschuur, 2002, 3D surface-related multiple prediction using sparse inversion: Experience with field data: 72nd Annual International Meeting, SEG, Expanded Abstracts, 2094–2097.

Zhou, B., I. M. Mason, and S. A. Greenhalgh, 1995, Accurate and efficient shot-gather dip moveout processing in the log-stretch domain: Geophysical Prospecting, **43**, 963–978.